LETTER

The trajectory, structure and origin of the Chelyabinsk asteroidal impactor

Jiří Borovička[1], Pavel Spurný[1], Peter Brown[2,3], Paul Wiegert[2,3], Pavel Kalenda[4], David Clark[2,3] & Lukáš Shrbený[1]

Earth is continuously colliding with fragments of asteroids and comets of various sizes. The largest encounter in historical times occurred over the Tunguska river in Siberia in 1908, producing[1,2] an airburst of energy equivalent to 5–15 megatons of trinitrotoluene (1 kiloton of trinitrotoluene represents an energy of 4.185×10^{12} joules). Until recently, the next most energetic airburst events occurred over Indonesia[3] in 2009 and near the Marshall Islands[4] in 1994, both with energies of several tens of kilotons. Here we report an analysis of selected video records of the Chelyabinsk superbolide[5] of 15 February 2013, with energy equivalent to 500 kilotons of trinitrotoluene, and details of its atmospheric passage. We found that its orbit was similar to the orbit of the two-kilometre-diameter asteroid 86039 (1999 NC43), to a degree of statistical significance sufficient to suggest that the two were once part of the same object. The bulk strength—the ability to resist breakage—of the Chelyabinsk asteroid, of about one megapascal, was similar to that of smaller meteoroids[6] and corresponds to a heavily fractured single stone. The asteroid broke into small pieces between the altitudes of 45 and 30 kilometres, preventing more-serious damage on the ground. The total mass of surviving fragments larger than 100 grams was lower than expected[7].

The data for Tunguska are limited to tree damage and records of seismic or acoustic waves at large distances. The Indonesia and Marshall Islands impacts were detected only by distant infrasonic stations or satellites in orbit and were therefore poorly documented. Some camera data exist for the multikiloton Sutter's Mill event[8], but precise analyses of the ablation process based on imaging have been made only for impacts of metre-sized bodies with energies of $\sim$0.1 kt trinitrotoluene[9–11] and less[12].

The Chelyabinsk impact occurred unexpectedly over a relatively densely populated Russian region during sunrise on 15 February 2013. The superbolide (an extremely bright meteor) generated a damaging air blast wave. An 8-m-wide hole in the ice of Lake Chebarkul, 70 km west of Chelyabinsk, was reported shortly after the event. Thousands of small meteorites of total mass >100 kg, classified as LL5 ordinary chondrites, were found in the areas south-southwest of Chelyabinsk[13].

Here we determine the bolide trajectory and orbit and describe the ablation process of the asteroid. The main data for these analyses were 15 bolide videos publicly available on the internet (Extended Data Table 1). We calibrated these videos with wide-field stellar imagery. Details of our procedure, which was based on the least-squares method[14], are given in Supplementary Information. The trajectory and speed of the bolide are presented in Table 1. The observed low deceleration provides an extreme lower limit of 10^6 kg for the mass of the body. The measured energy[5] and speed provide a best estimate of the mass of $\sim$1.2 $\times$ 10^7 kg, corresponding to a diameter of $\sim$19 m assuming a bulk density of 3,300 kg m^{-3}.

The pre-impact orbit (Table 2) is consistent with an origin in the main asteroid belt, most probably in the inner main belt near the ν_6 secular resonance. We integrated the orbit and 1,000 test particles within the orbital uncertainties (a probability cloud) 2,000 years into the past. The asteroid spent the six weeks before impact within an elongation of 45°

from the Sun, a region of the sky inaccessible to ground-based telescopes. At earlier times, the asteroid was always too faint to be seen when some portion of the probability cloud was in the field of view of existing asteroid surveys. We note that the 2.2-km-diameter[15] near-Earth asteroid 86039 (1999 NC43) of spectral type Q[16] (corresponding to ordinary chondrites) has a very similar orbit, with very low dissimilarity criteria, $D = 0.050$ (ref. 17) and $D' = 0.018$ (ref. 18), relative to Chelyabinsk asteroid. Though this does not provide an unequivocal dynamical link, such a close match is unlikely statistically. We expect 227 near-Earth asteroids brighter than 86039 to exist[19]. Selecting at random from the expected distribution of near-Earth asteroids[20], it takes an average of 6×10^5 draws before selecting one with a smaller D value, and more than 3×10^6 draws before selecting one with a smaller D' value. Because 227/600,000 and 227/3,000,000 are equivalent to 1:2,600 and 1:13,000, respectively, we conclude that there is an approximately 1:10,000 chance that the proximity of these orbits is due purely to chance. The two orbits have maintained two intersection points over the past 2,000 years, one near perihelion and one near aphelion (Extended Data Fig. 1). The minimum velocity kick required to eject the Chelyabinsk asteroid from 86039 is 0.7 km s^{-1} (aphelion) or 2 km s^{-1} (perihelion). This ejection velocity is consistent with a collision with another asteroid (which would provide a kick of a few kilometres per second).

The fragmentation during atmospheric entry was studied using the bolide light curve[5] and deceleration with a procedure developed recently[11]. The arrival times of secondary sonic booms heard on videos were also used to locate fragmentation points (the primary blast wave was caused by the cylindrical shock from the trajectory[5]). The dynamic pressure

Table 1 | Trajectory of the Chelyabinsk superbolide

Time (s)	Longitude (°)	Latitude (°)	Height (km)	Speed (km s^{-1})
1.07	64.477	54.454	95.0	19.03
6.97	62.888	54.664	60.0	19.05
10.46	61.933	54.780	40.0	19.03
12.24	61.442	54.837	30.0	18.9
13.18	61.193	54.864	25.0	18.0
14.18	60.943	54.892	20.0	14.2
15.17	60.802	54.907	17.2	6
		Fragment F1		
14.32	60.945	54.893	20.0	13.5
16.04	60.704	54.922	15.0	6.4
17.80	60.5883	54.9361	12.57	3.2

Time zero corresponds to approximately 3:20:20 UT. Coordinates are given in the WGS84 geoid system. Speed is relative to the Earth's surface. At the beginning, the acceleration due to gravity was larger than deceleration due to atmospheric drag. The beginning speed (19.03 ± 0.13 km s^{-1}) remained constant to within 0.02 km s^{-1} down to an altitude of 35 km. The bolide was recorded in the analysed videos between altitudes of 95.1 and 12.6 km, over a trajectory of total length 272 km. The apparent radiant was changing owing to Earth's gravity, starting at right ascension α = 21 h 53 min 7 s ± 24 s (328.28° ± 0.10°) and declination δ = +7° 28′ ± 3′ (+7.47° ± 0.05°) at altitude 95 km and changing to α = 21 h 51 min 58 s (327.99°), δ = +7° 53′ (7.88°) at altitude 20 km. These values correspond to a local radiant azimuth of A = 103.50° ± 0.09° (east of north) and elevation h = 18.55° ± 0.08°, and, respectively, A = 100.63° and h = 16.95° (we note that A and h change also as a result of Earth's curvature). For comparison, the radiant of fragment F1 at 20 km was A = 101.87° ± 0.4°, h = 17.53° ± 0.3°.

[1]Astronomical Institute, Academy of Sciences of the Czech Republic, CZ-251 65 Ondřejov, Czech Republic. [2]Department of Physics and Astronomy, University of Western Ontario, London, Ontario N6A 3K7, Canada. [3]Centre for Planetary Science and Exploration, University of Western Ontario, London, Ontario N6A 5B7, Canada. [4]Institute of Rock Structure and Mechanics, Academy of Sciences of the Czech Republic, V Holešovičkách 41, CZ-18209 Praha 8, Czech Republic.

Table 2 | Pre-impact orbit of Chelyabinsk asteroid and the orbit of asteroid 86039 (1999 NC43)

	Chelyabinsk	86039
Semimajor axis, a (AU)	1.72 ± 0.02	$1.759621064 \pm 6 \times 10^{-9}$
Perihelion distance, q (AU)	0.738 ± 0.002	$0.7403896 \pm 1 \times 10^{-7}$
Eccentricity, e	0.571 ± 0.006	$0.57923346 \pm 6 \times 10^{-8}$
Inclination, i (°)	4.98 ± 0.12	$7.12312 \pm 1 \times 10^{-5}$
Longitude of the ascending node, Ω (°)	326.459 ± 0.001	$311.81880 \pm 5 \times 10^{-5}$
Argument of perihelion, ω (°)	107.67 ± 0.17	$120.55894 \pm 5 \times 10^{-5}$
Time of perihelion passage	2012 December 31.39 ± 0.17	2014 January $17.45565 \pm 2 \times 10^{-5}$

The geocentric radiant and velocity of Chelyabinsk were $\alpha_g = 22$ h 11 min 17 s $\pm$ 26 s (332.82 $\pm$ 0.11°), $\delta_g = +0°17' \pm 8'$ ($+0.28° \pm 0.14°$), $v_g = 15.14 \pm 0.16$ km s^{-1}. The orbit was obtained by numerical integration back in time to 60 d pre-impact, with the RADAU integrator[28,29]. The orbit of 86039 was taken from NASA JPL Database (http://ssd.jpl.nasa.gov/sbdb.cgi) on 7 June 2013. All angular coordinates are in equinox J2000.0.

acting on the body was computed at each fragmentation point to evaluate the mechanical strength of the body.

The first significant mass loss occurred at an altitude of about 45 km, under a dynamic pressure of 0.7 MPa. The series of most severe fragmentations occurred at altitudes between 40 and 30 km (1–5 MPa). Acoustic analysis revealed 11 individual fragmentations between altitudes 39.2 and 29.8 km (Extended Data Fig. 2), the two strongest at 31.9 and 30.6 km, respectively (with uncertainties of ± 0.3 km). By 29 km, the asteroid had already fragmented into about 20 large boulders of masses $\sim 10^4$ kg. Judging from the deceleration, the mass of the leading boulder (main body) was $\sim 2 \times 10^4$ kg. The boulders started to break up again at altitudes of 26–24 km (10–13 MPa). The main body remained intact and quite massive ($\sim 10^4$ kg) until an altitude of 22 km, before severe disintegration began at a pressure of 18 MPa. Only a 15-kg fragment remained from the leading main mass at 17 km. Fragment F1, the largest individual piece surviving the descent, separated from one of the more decelerated boulders (not the main body) at an altitude of about 25 km, surviving a maximal dynamic pressure of 15 MPa at 20 km. Its trajectory deviated from the original direction of flight (Extended Data Fig. 3) by $1.3° \pm 0.4°$, implying that the lateral velocity gained at the break-up was 400 ± 130 m s^{-1}. This lateral velocity is almost an order of magnitude larger than aerodynamic theory[21] and laboratory experiments[22] predict. Nevertheless, it is similar to the behaviour of the Morávka bolide[10], suggesting that forces other than purely aerodynamic effects are also present during the fragmentation of bolides. Judging from its deceleration, the terminal mass of fragment F1 was 450 ± 50 kg and dark-flight computation predicts a landing point in Lake Chebarkul, within 300 m of the actual impact site (Extended Data Fig. 4). The predicted

impact points and masses of other observed fragments (Extended Data Fig. 5) are given in Fig. 1 and Extended Data Fig. 6. Judging from the light-curve shape, the total mass of surviving fragments >100 g was at most only several per cent of the original mass and probably much less. It is much less that the pancake model predicts (>50%) and less than the separated-fragments model predicts[7] (>10%).

The fragmentation history shows that the bulk strength of the Chelyabinsk asteroid was ~ 1 MPa, a value typical for smaller meteoroids, confirming that for near-Earth objects there is little correlation between strength and size on scales from centimetres to tens of metres[6]. Only the very strongest parts, representing <1% of the original mass, had strength >15 MPa, which may be comparable to the exceptionally strong Carancas meteoroid[23,24] and typical tensile strengths of recovered stony meteorites[6]. Even in the Martian atmosphere, the body would probably separate into several large fragments before reaching the surface. It is therefore not surprising that most fresh craters on Mars are found in clusters[25].

A large dust trail was left in the atmosphere after the bolide passage. The southern and bottom sides of the trail were illuminated by the rising Sun. From northern sites the trail looked thin because only the illuminated bottom was visible, except for the first seconds, when the trail was self-luminous. The trail started at an altitude of 68 km. Between 60 and 26 km, the trail was thick, with radius 1.0–1.8 km. A thinner trail continued to 21.5 km and a very thin part extended to 18 km. The total volume of the trail was of order 600 km^3 and its air mass was $\sim 5 \times 10^9$ kg. The lower edge of the thick trail was almost stationary immediately after the passage of the bolide but then moved forwards in two waves as the material originally released at higher heights arrived. The velocities of these shocks were 2.8 and 1.7 km s^{-1}, respectively
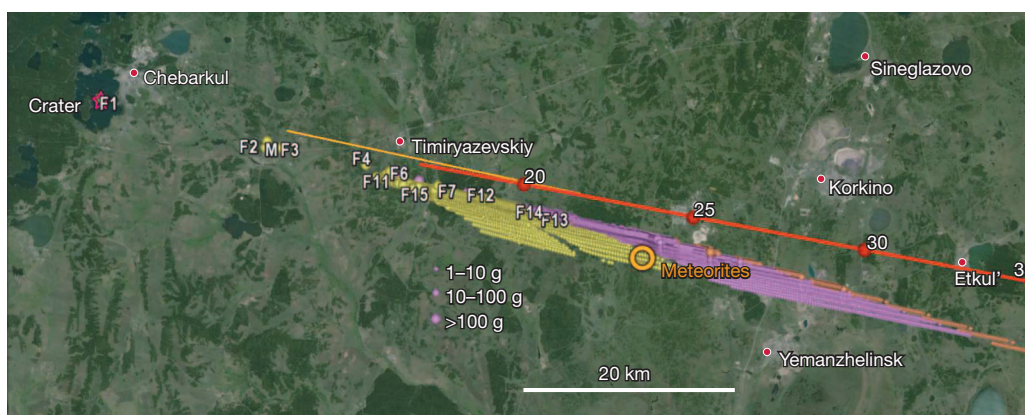
Figure 1 | Ground projection of the terminal part of the bolide trajectory and meteorite-strewn field. Main trajectory (thick red line) and trajectory of fragment F1 (thin orange line) as plotted on Google Earth. The marks denote altitudes in kilometres. The predicted impact positions of 11 observed fragments (F1–F4, F6, F7 and F11–F15) are shown. The impact positions of simulated small (non-observable) fragments are also given. Yellow dots denote fragments that separated at lower altitude (21–26 km), pink fragments originate in the main break-ups at 30–39 km and brown fragments are from break-ups above 40 km. The three dot sizes correspond to terminal masses of 1–10 g, 10–100 g and >100 g. The second largest fragment, F2, had an estimated mass of 30 kg based on its observed deceleration. The dynamics after

luminous flight ceased[30] (dark flight) was computed using the wind field from the nearest available radiosonde at Verkhnee Dubrovo (180 km north of Chelyabinsk) measured at 0:00 UT on 15 February 2013. Using the wind field measured by radiosonde at Kurgan (250 km east of Chelyabinsk) would shift the meteorites much more to the south (by 2.5 km for a 200-g meteorite). The position of the impact hole in Lake Chebarkul (marked 'Crater') and the centroid of strewn field of small meteorites[13] are also shown. See also Extended Data Fig. 4. We expect that, as in other cases[11], the mass distribution will be more complicated and the strewn field will be larger than our idealized model predicts.

(Extended Data Fig. 6). Larger regions of hot material within the trail continued moving forwards for some time after the bolide passage. The forward velocity of the brightest (and lowest) of several distinct hotspots (Extended Data Fig. 7) decreased from 0.7 to 0 km s^{-1} during the period 1.5–4 s after the passage of the body. At the same time, a constant vertical velocity of 0.08 km s^{-1} was measured for this hotspot (Extended Data Fig. 6). The upward motion, caused by buoyancy of the hot mixture of air, vapour and dust, continued when the forward motion stopped. About 15 s after the bolide passage, splitting of the trail into two parallel tracks became apparent (Extended Data Fig. 8), an effect seen in high-altitude luminous meteor trails and caused by convective instability leading to vortices[26]. After 50 s, the top of the cloud, which formed from the hotspot, was 3 km above the bottom of the trail (the trail as a whole moved about 0.5 km upwards). The maximum height of 6–7 km was reached after 3 min (Extended Data Fig. 9).

On the basis of the fragmentation strength of the Chelyabinsk asteroid, we conclude that it was probably a fractured single stone and not a rubble-pile assemblage, whose expected strength would be only ~25 Pa (ref. 27). The unusually close orbital association with asteroid 86039 suggests a possible genetic connection. Detailed comparison of reflectance spectra from the Chelyabinsk meteorite and 86039 are highly desirable to help explore this relationship. If the orbital association is real, we would also predict a very short exposure age for Chelyabinsk relative to other LL chondrites, because such orbital associations can only persist for a small fraction of the dynamical lifetime of an near-Earth asteroid.
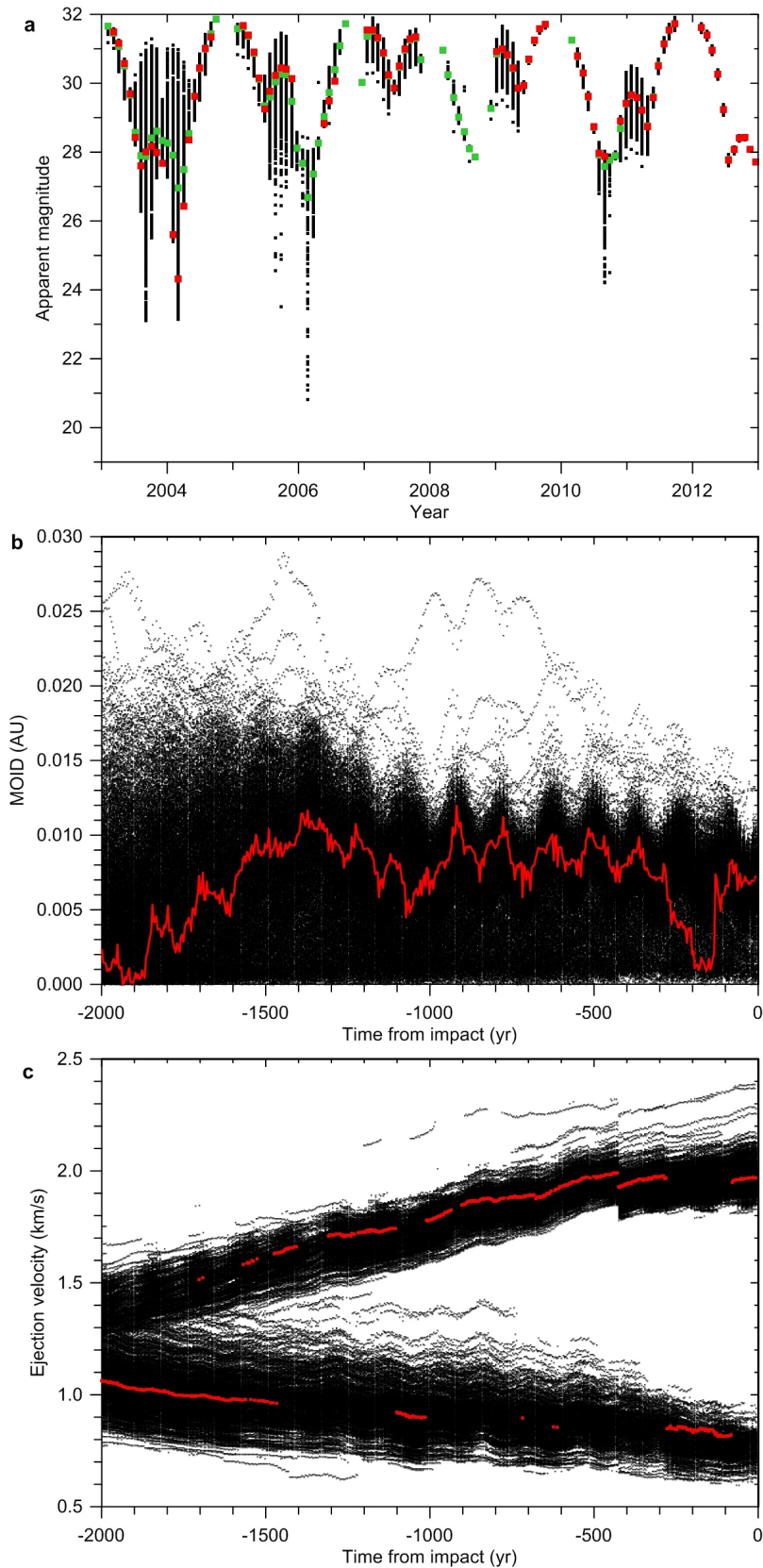
1. Vasilyev, N. V. The Tunguska meteorite problem today. *Planet. Space Sci.* **46,** 129–150 (1998).
2. Boslough, M. B. E. & Crawford, D. A. Low altitude airbursts and the impact threat. *Int. J. Impact Eng.* **35,** 1441–1448 (2008).
3. Silber, E. A., Le Pichon, A. & Brown, P. G. Infrasonic detection of a near-Earth object impact over Indonesia on 8 October 2009. *Geophys. Res. Lett.* **38,** L12201 (2011).
4. McCord, T. B. *et al.* Detection of a meteoroid entry into the Earth's atmosphere on February 1, 1994. *J. Geophys. Res.* **100** (E2), 3245–3249 (1995).
5. Brown, P. G. *et al.* A 500-kiloton airburst over Chelyabinsk and an enhanced hazard from small impactors. *Nature* http://dx.doi.org/10.1038/nature12741 (this issue).
6. Popova, O. *et al.* Very low strengths of interplanetary meteoroids and small asteroids. *Meteorit. Planet. Sci.* **46,** 1525–1550 (2011).
7. Bland, P. A. & Artiemeva, N. A. Efficient disruption of small asteroids by Earth's atmosphere. *Nature* **424,** 288–291 (2003).
8. Jenniskens, P. *et al.* Radar-enabled recovery of the Sutter's Mill meteorite, a carbonaceous chondrites regolith breccia. *Science* **338,** 1583–1587 (2012).
9. Borovička, J., Popova, O. P., Nemtchinov, I. V., Spurný, P. & Ceplecha, Z. Bolides produced by impacts of large meteoroids into the Earth's atmosphere: comparison of theory with observations. I. Benešov bolide dynamics and fragmentation. *Astron. Astrophys.* **334,** 713–728 (1998).
10. Borovička, J. & Kalenda, P. The Morávka meteorite fall: 4. Meteoroid dynamics and fragmentation in the atmosphere. *Meteorit. Planet. Sci.* **38,** 1023–1043 (2003).
11. Borovička, J. *et al.* The Košice meteorite fall: atmospheric trajectory, fragmentation, and orbit. *Meteorit. Planet. Sci.* http://dx.doi.org/10.1111/maps.12078 (17 April 2013).
12. Spurný, P. *et al.* The Bunburra Rockhole meteorite fall in SW Australia: fireball trajectory, luminosity, dynamics, orbit, and impact position from photographic and photoelectric records. *Meteorit. Planet. Sci.* **47,** 163–185 (2012).
13. Nazarov, M. A. Chelyabinsk. *Meteorit. Bull.* **102** (2013).
14. Borovička, J. The comparison of two methods of determining meteor trajectories from photographs. *Bull. Astron. Inst. Czechoslovakia* **41,** 391–396 (1990).
15. Delbó, M., Harris, A. W., Binzel, R. P., Pravec, P. & Davies, J. K. Keck observations of near-Earth asteroids in the thermal infrared. *Icarus* **166,** 116–130 (2003).
16. Binzel, R. P. *et al.* Observed spectral properties of near-Earth objects: results for population distribution, source regions, and space weathering processes. *Icarus* **170,** 259–294 (2004).
17. Southworth, R. B. & Hawkins, G. S. Statistics of meteor streams. *Smithsonian Contrib. Astrophys.* **7,** 261–285 (1963).
18. Drummond, J. D. A test of comet and meteor shower associations. *Icarus* **45,** 545–553 (1981).
19. Mainzer, A. *et al.* NEOWISE observations of near-Earth objects: preliminary results. *Astrophys J.* **743,** 156 (2011).
20. Bottke, W. F. Jr *et al.* Debiased orbital and absolute magnitude distribution of the near-Earth objects. *Icarus* **156,** 399–433 (2002).
21. Artemieva, N. A. & Shuvalov, V. V. Motion of fragmented meteoroid through the planetary atmosphere. *J. Geophys. Res.* **106** (E2), 3297–3309 (2001).
22. Park, C. & Brown, J. D. Fragmentation and spreading of a meteor-like object. *Astron. J.* **144,** 184 (2012).
23. Brown, P. *et al.* Analysis of a crater-forming meteorite impact in Peru. *J. Geophys. Res.* **113,** E09007 (2008).
24. Borovička, J. & Spurný, P. The Carancas meteorite impact: encounter with a monolithic meteoroid. *Astron. Astrophys.* **485,** L1–L4 (2008).
25. Daubar, I. J., McEwen, A. S., Byrne, S., Kennedy, M. R. & Ivanov, B. The current Martian cratering rate. *Icarus* **225,** 506–516 (2013).
26. Kelley, M. C., Williamson, C. H. K. & Vlasov, M. N. Double laminar and turbulent meteor trails observed in space and simulated in the laboratory. *J. Geophys. Res.* **118,** 3622–3625 (2013).
27. Sánchez, P. & Scheeres, D. J. The strength of regolith and rubble pile asteroids. Preprint at http://arxiv.org/abs/1306.1622 (2013).
28. Everhart, E. in *Dynamics of Comets: Their Origin and Evolution* (eds Carusi, A. & Valsecchi, G.) 185 (Kluwer, 1985).
29. Clark, D. & Wiegert, P. A numerical comparison with the Ceplecha analytical meteoroid orbit determination method. *Meteorit. Planet. Sci.* **46,** 1217–1225 (2011).
30. Ceplecha, Z. Geometric, dynamic, orbital and photometric data on meteoroids from photographic fireball networks. *Bull. Astron. Inst. Czechoslovakia* **38,** 222–234 (1987).

Extended Data Figure 1 | Visibility and orbital evolution of Chelyabinsk asteroid in the past. The results of backward integration of Chelyabinsk nominal orbit (red) and its 1,000 clones (black dots). **a**, Apparent magnitude as seen from the Earth at 30-day intervals during past 10 years. Green, mean of all clones. Plotted only for elongations >45° from the Sun. **b**, Minimum orbit intersection distance (MOID) between the Chelyabinsk orbit and the osculating orbit of asteroid 86039 during the past 2,000 years. **c**, Change in velocity required to reach Chelyabinsk orbit from the orbit of 86039 at MOID during the past 2,000 years.
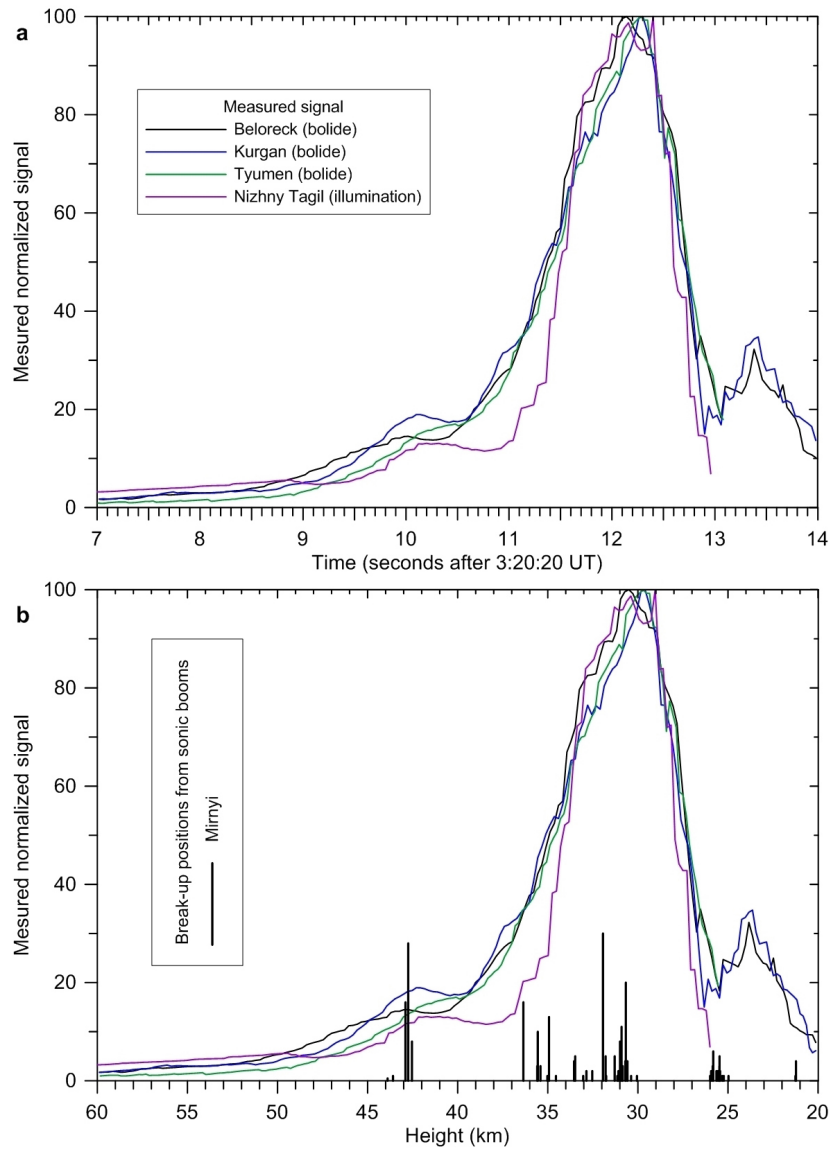
c

Heights of break-ups from sonic booms at 19 videos

42.7‡ - *39.2*† - *37.2*† - 36.4 - 35.5 - 34.9 - 33.5 - 32.6 - **31.9*** - 30.9 - **30.6*** - 29.8

25.8 - 25.5 - 21.3 - *18.6*† - *17.5*†

*strong
†not confirmed on video A19
‡only on video A19 but confirmed on seismic station BRVK. Another break-up suggested
 by BRVK at ~ 47 km.

Extended Data Figure 2 | Light curve of Chelyabinsk superbolide in relative units and fragmentation altitudes as determined from sonic booms. The luminous signal was computed in relative units from pixel sum values from substantial parts of the images, and then normalized to 100. Corrections to bolide range and atmospheric extinction were applied but no attempt to convert the signal to absolute units was made (for the absolute light curve, see ref. 5). For each video, the measured pixel sum was corrected using the estimated changes of automatic gain control of the camera. The absolute timing was obtained from the Nizhny Tagil video (L1) and the height scale from the Beloreck video (video 14, or L4). The fragmentation altitudes were determined from the timing of secondary sonic booms and numerical ray-tracing modelling of the sonic wave's propagation from the bolide to the video sites. The videos used are listed in Extended Data Table 1. **a**, Bolide light curve as a function of time. **b**, The same data as a function of height compared with the computed source heights of sonic booms detected (as image failures) in the Mirnyi video (A19). The fragmentations are marked by vertical bars at the corresponding height. The length of the bar is proportional to the number of video frames affected by the failure. **c**, The compilation of sonic boom source heights from all 19 videos used for acoustic analysis.
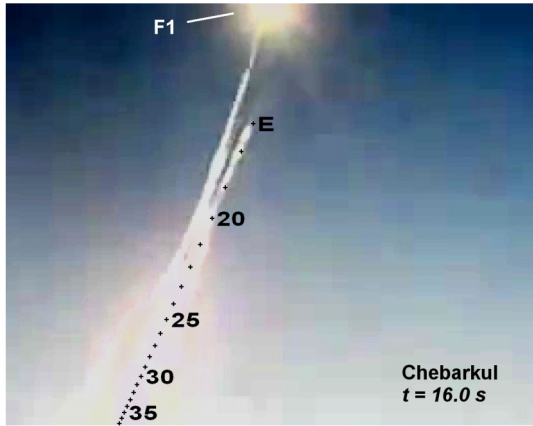
Extended Data Figure 3 | Deviation of fragment F1 from the main trajectory. Frame from video 15. The time is counted from 3:20:20 UT. The labelled marks identify points on the main trajectory at the given altitude (in kilometres). E represents the endpoint of the main trajectory.

Extended Data Figure 4 | Predicted impact position of fragment F1, computed with four different wind fields, compared with the position of the hole in the ice ('Crater'). The point marked F1 was computed with Verkhnee Dubrovo radiosonde data (0:00 UT). Point K is for Kurgan radiosonde (0:00 UT), point U is for the UKMO wind model for Chelyabinsk (12:00 UT) and point G is for the G2S model (3:00 UT) (ref. 31 in Supplementary Information). The distance between U and K is 960 m. The distance between F1 and the crater is 220 m. We note that the position of the crater was not used for the computation of the F1 trajectory and impact point. The background image is from Google Earth and was taken one day after the impact.

Extended Data Figure 5 | Identification of fragments in a series of images from video 7. Fragments F1–F7 originated at lower altitudes (~25 km), whereas fragments F11–F16 originated at higher altitudes (>30 km).

Fragment	Longitude °E	Latitude °N	Ablation coeff., s²/km²	Terminal mass, kg
M	60.5635	54.9209	0.04	15
F1	60.3194	54.9615	0.01	450
F2	60.5662	54.9268	0.05	30
F3	60.5861	54.9211	0.03	20
F4	60.7113	54.9071	0.14	3
F5	60.7572	54.8991	0.06	1
F6	60.7466	54.9019	0.05	2
F7	60.8170	54.8903	0.35	0.5
F11	60.7597	54.8980	0.09	5
F12	60.8598	54.8843	0.03	1.5
F13	60.9681	54.8666	?	0.2
F14	60.9309	54.8730	0.005	0.5
F15	60.7893	54.8945	?	5
F16	60.9583	54.8692	0.08	0.3

Extended Data Figure 6 | Dynamics of the dust trail and fragments and predicted impact positions of observed fragments. a, Altitude as a function of time for the lower edge of the thick dust trail (TE) and hotspots within the trail (HS1–HS3). The hotspots are identified in Extended Data Fig. 7. **b**, Altitude as a function of time for the main body (M), lower fragments (F1–F7) and upper fragments (F11–F16), plotted together with the dust trail features. The fragments are identified in Extended Data Fig. 5. The main body and trail were measured primarily from video 2; and the fragments, from video 7.

c, Upward motion of the main hotspot (HS1) within the dust trail. Vertical deviation of the centre of the hotspot from the trajectory is plotted against time. The linear fit gives upward velocity of 0.08 km s⁻¹. **d**, Predicted impact positions and dynamic properties of observed fragments. Ablation coefficients and terminal masses were obtained by fitting the observed decelerations. Masses are valid for assumed spherical shapes and bulk densities of 3,300 kg m⁻³. In some cases, the ablation coefficient could not be computed because there was an insufficient number of data points.

Extended Data Figure 7 | Images of the dust trail at early stages. a–c, Images from a single video site (video 2) located north of the fireball trajectory. Time is counted from 3:20:20 UT. Three distinct hotspots (HS1–HS3) are identified. The labelled marks identify points on the 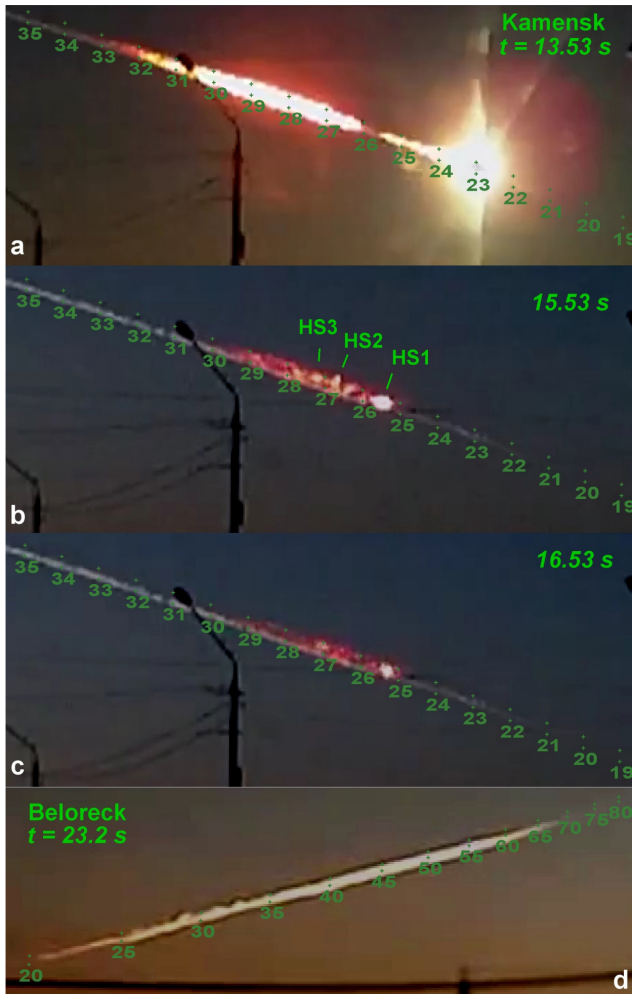trajectory at the given altitude (in kilometres). The unlabelled marks above them identify points at the same geographic coordinates but 1 km higher. They are provided to assess the width of the trail. **d,** Image from video 14, from the southwest. It demonstrates that the width of the fully illuminated fresh trail was ~2 km over much of its length. For later evolution of the trail, see Extended Data Figs 8 and 9.
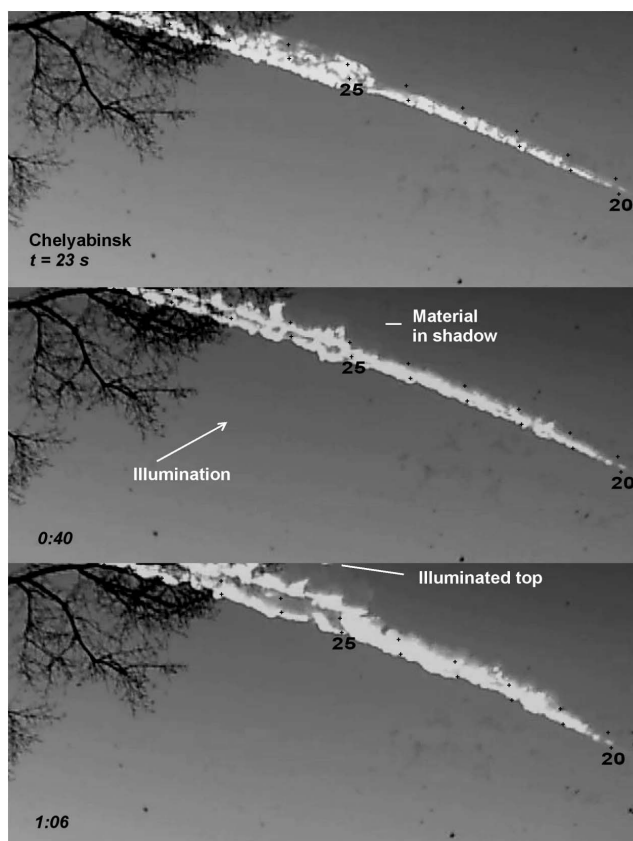
Extended Data Figure 8 | Evolution of the lower part of the dust trail as seen from Chelyabinsk during the first minute. Three frames from video 6 (the video has colour defects). The time is given in minutes and seconds and is counted from 3:20:20 UT. The lower marks identify points on the trajectory in 1-km altitude intervals. The upper marks identify points at the same geographic coordinates but 1 km higher. The video demonstrates vertical ascent and splitting of the trail. When the original video is speeded up, rotation of the material in the trail is clearly visible. The trail was illuminated from below. The 'bubble' formed at the position of the main hotspot (HS1; see Extended Data Fig. 7) was in shadow most of the time. Only its illuminated top is visible on the third frame, just at the edge of the field of view.

Extended Data Figure 9 | Longer-term evolution of the dust trail.
Five frames from an uncalibrated video (http://www.youtube.com/
watch?v=Z20lnOVscpc, author D. Beletsky) taken from south of the fireball
trajectory (on the road from Magnitogorsk to Chelyabinsk). The time is given
in minutes and seconds and is counted from 3:20:20 UT. The trail was fully
illuminated from this site. The video demonstrates the rise of the 'bubble'
formed at the position of the main hotspot (HS1; see Extended Data Fig. 7). The
maximum altitude was reached about 3 min after the bolide had passed by.

Extended Data Table 1 | List of YouTube videos used

Extended Data Table 1 | List of used YouTube videos

No.	City	Longitude °E	Latitude °N	Altitude m	YouTube code*	Author
		Videos used for trajectory determination				
1	Verkhnyaya Pyshma	60.6082	56.9635	276	LzvipPOpUy0	Vos'moy Rayon
2	Kamensk Ural'sky	61.9186	56.4151	170	kFlpCT3v12E	Aleksandr Ivanov
3	Kamensk Ural'sky	61.9333	56.3933	151	7TPDwSXaiB0	LANCER96RUS
4	Kamensk Ural'sky	61.9426	56.3852	163	J3DqsbxKOMA	LANCER96RUS
5	Chelyabinsk	61.2967	55.2204	246	4ZxXYscmgRg	Andrey Borisovich Korolev
6	Chelyabinsk	61.4720	55.1797	231	OM-5ngYg5Mg	Vyacheslav Kravchenko
7	Chelyabinsk	61.3935	55.1756	228	8Eu7QAP2DPM	Viktor Borzov
8	Chelyabinsk	61.4448	55.1663	231	32aJ4RB8Mql	MegaProfitroll
9	Chelyabinsk	61.3637	55.1500	257	gQ6Pa5Pv_io	Dmitriy Volkov
10	Korkino	61.3995	54.8909	241	odKjwrjIM-k	nek rozato
11	Yemanzhelinsk	61.3040	54.7566	234	2Gc1HgO5hNY	Aleksandr Zakharov
12	Kichigino	61.2717	54.5008	238	0CoP7WB8Gew	Mikhail Troitsk
13	Troitsk	61.5313	54.0771	183	UjNpJXP7trQ	C2Crash
14	Beloreck	58.4102	53.9527	532	5_1ytDqps8A	MrKuzaman
15	Chebarkul	60.4002	54.9950	343	xboo7LiNR08	yulya Ryzhaya
		Videos used for light curve measurement				
L1	Nizhny Tagil	59.9439	57.8703	220	NcZNhJVW5xl[†]	SetiTagila
L2	Tyumen'	65.6053	57.2024	60	1ZdYf2vM5LA	EastSide287
L3	Kurgan	65.2956	55.4735	70	X2ja6_zJtzk	Dmitriy Grekov
L4	Beloreck	58.4102	53.9527	532	5_1ytDqps8A	MrKuzaman
		Videos used for acoustic analysis				
A1	Chelyabinsk	55.1647	61.5482		HaMurqKMenw	Alexandr Gubarev
A2	Malinovka	55.0900	61.2500		5Rh2-v-gFEs	Svladislav74
A3	Pervomaysky	54.8726	61.2008		R99zvcrqXo8	Axel Alex
A4	Chelyabinsk	55.2675	61.4082		hMZkv0-2500	NIKI4174
A5	Chelyabinsk	55.1799	61.3479		5xMOSY4bW_M	Aleksej D
A6	Chelyabinsk	55.1570	61.3657		uXU3z3-bxNk	Andrey Yurkin
A7	Chelyabinsk	55.1500	61.3637		gQ6Pa5Pv_io	Dmitriy Volkov
A8	Chelyabinsk	55.1114	61.3509		Np_mpGYSBSA	Serg Kh
A9	Chelyabinsk	55.1650	61.4070		rflTN4XAt34	Maxim Savelyev
A10	Chelyabinsk	55.1582	61.4113		G2KpK_GmvA8	Yuriy Bazhaev
A11	Chelyabinsk	55.1570	61.4452		38zQkZCWIL0	Sergey Polyakov
A12	Chelyabinsk	55.1636	61.4703		zkVUbMdAV2Q	Alexandr Burlakov
A13	Chelyabinsk	55.1665	61.4639		QTZ0vesq5fA	greshnikacw
A14	Yemanzhelinsk	54.7564	61.3280		KmjjGgvOlMY	Daniil Lysenko
A15	Chelyabinsk	55.1404	61.4780		16KxOxjSndA	dima stepanov
A16	Kopeysk	55.1210	61.6046		VZJEfNld_JU	Aleksandr Al'shevsky
A17	Kopeysk	55.1103	61.6042		4x3xG-eKpNA	ZaTDro
A18	Kopeysk	55.1087	61.6183		UsOEy5hCCow	Andrey Kostomarov
A19	Mirnyi	54.577	60.312		LmlwWFDylx0	kaban0796

* http://www.youtube.com/watch?v=*code*
[†] The last of the four videos in the compilation was used